

UC Berkeley

UC Berkeley Previously Published Works

Title

Controlling structure and interfacial interaction of monolayer TaSe₂ on bilayer graphene.

Permalink

<https://escholarship.org/uc/item/4h36k7s2>

Journal

Nano Convergence, 11(1)

Authors

Lee, Hyobeom

Im, Hayoon

Choi, Byoung

et al.

Publication Date

2024-04-15

DOI

10.1186/s40580-024-00422-9


Peer reviewed

FULL PAPER

Open Access



Controlling structure and interfacial interaction of monolayer TaSe₂ on bilayer graphene

Hyobeom Lee^{1†}, Hayoon Im^{2†}, Byoung Ki Choi³, Kyoungree Park¹, Yi Chen^{4,5,6,7}, Wei Ruan^{4,8}, Yong Zhong^{10,9}, Ji-Eun Lee^{11,3}, Hyejin Ryu¹², Michael F. Crommie^{13,4}, Zhi-Xun Shen^{10,9}, Choongyu Hwang^{2*} , Sung-Kwan Mo^{3*} and Jinwoong Hwang^{1*}

Abstract

Tunability of interfacial effects between two-dimensional (2D) crystals is crucial not only for understanding the intrinsic properties of each system, but also for designing electronic devices based on ultra-thin heterostructures. A prerequisite of such heterostructure engineering is the availability of 2D crystals with different degrees of interfacial interactions. In this work, we report a controlled epitaxial growth of monolayer TaSe₂ with different structural phases, 1*H* and 1*T*, on a bilayer graphene (BLG) substrate using molecular beam epitaxy, and its impact on the electronic properties of the heterostructures using angle-resolved photoemission spectroscopy. 1*H*-TaSe₂ exhibits significant charge transfer and band hybridization at the interface, whereas 1*T*-TaSe₂ shows weak interactions with the substrate. The distinct interfacial interactions are attributed to the dual effects from the differences of the work functions as well as the relative interlayer distance between TaSe₂ films and BLG substrate. The method demonstrated here provides a viable route towards interface engineering in a variety of transition-metal dichalcogenides that can be applied to future nano-devices with designed electronic properties.

Keywords Transition metal dichalcogenides, TaSe₂, Graphene, Interface, Heterostructure, Molecular beam epitaxy, Angle-resolved photoemission spectroscopy, Scanning tunneling microscopy

[†]Hyobeom Lee and Hayoon Im contributed equally to this work.

*Correspondence:

Choongyu Hwang
ckhwang@pusan.ac.kr

Sung-Kwan Mo
skmo@lbl.gov

Jinwoong Hwang
jwhwang@kangwon.ac.kr

¹ Department of Physics and Institute of Quantum Convergence Technology, Kangwon National University, Chuncheon, South Korea

² Department of Physics, Pusan National University, Busan, South Korea

³ Advanced Light Source, Lawrence Berkeley National Laboratory, Berkeley, CA, USA

⁴ Department of Physics, University of California, Berkeley, CA, USA

⁵ International Center for Quantum Materials, School of Physics, Peking University, Beijing 100871, China

⁶ Collaborative Innovation Center of Quantum Matter, Beijing 100871, China

⁷ Interdisciplinary Institute of Light-Element Quantum Materials and Research Center for Light-Element Advanced Materials, Peking University, Beijing 100871, China

⁸ State Key Laboratory of Surface Physics, New Cornerstone Science Laboratory, and Department of Physics, Fudan University, Shanghai, China

⁹ Geballe Laboratory for Advanced Materials, Department of Physics and Applied Physics, Stanford University, Stanford, CA, USA

¹⁰ Stanford Institute for Materials and Energy Sciences, SLAC National Accelerator Laboratory, Menlo Park, CA, USA

¹¹ Max Planck POSTECH Center for Complex Phase Materials, Pohang University of Science and Technology, Pohang, South Korea

¹² Center for Spintronics, Korea Institute of Science and Technology, Seoul, South Korea

¹³ Materials Sciences Division, Lawrence Berkeley National Laboratory, Berkeley, CA, USA

1 Introduction

The exotic properties of atomically thin two-dimensional (2D) crystals, first revealed in graphene, have led to a tremendous expansion in the 2D materials research [1–4]. In particular, controllable atomic layer-by-layer growth using chemical vapor deposition and molecular beam epitaxy (MBE) has allowed us to address fundamental issues in the 2D limit and to search for artificial interfaces with designed functionalities [2, 3, 5–8]. Transition-metal dichalcogenides (TMDCs) provide a fertile platform to realize a number of exotic properties with various constituent atoms and crystal structures [1–3, 5], e.g., $1H$ (trigonal prismatic coordination) and $1T$ (octahedral coordination) with differences in the coordination of six chalcogen atoms surrounding a metal atom. One caveat, and simultaneously an advantage of 2D crystals, is that the intrinsic physical properties of epitaxially grown monolayer (ML) TMDC films can be modified by strong interactions with a substrate [9–13]. Bilayer graphene (BLG) on a SiC(0001) substrate has been ubiquitously used for the epitaxial growth of layered 2D materials when studying the intrinsic characteristics of van der Waals (vdW) materials in a 2D limit due to relative chemical inertness of BLG [14–18]. The weak interactions between BLG and epitaxial vdW materials can preserve the intrinsic properties of overlaid 2D materials. Indeed, the formation of novel ground states has been demonstrated in TMDCs by using BLG substrate, e.g., the indirect-to-direct band gap transition in $2H$ -MoSe₂ [14], the exciton condensed states in ML $1T$ -ZrTe₂ [15], the quantum spin Hall state in ML $1T$ -WTe₂ [16], and metal-to-insulator transition in $1T$ -IrTe₂ [17].

Among the family of TMDCs, MBE-grown MX₂ (M = Nb, Ta; X = S, Se) on a BLG substrate has been intensively studied, and the growth recipes have been well established [19], making them a great platform to study exotic quantum phenomena in the ML regime. Examples include charge density waves (CDW) and Ising superconductivity in $1H$ -MX₂ [20–22], exotic orbital textures with Mott insulating states and quantum spin liquid behavior in $1T$ -MX₂ [23–25], and heavy fermionic behaviors in $1T/1H$ -MX₂ heterostructures [24–28]. One critical aspect to consider but often neglected is that BLG substrate may give a significant charge transfer to the overlaid MX₂ films due to a substantial difference in work functions between MX₂ and BLG, which may strongly affect the intrinsic properties of ML MX₂ [29–31]. Considering that the ground states of atomically thin TMDC films can be easily modified by the amount of extra charge doping [11, 15, 32], it is crucial to carefully study the effect of the BLG substrate on overlaid ML MX₂ films.

Here, we report the electronic structure of epitaxially grown ML TaSe₂ films on a BLG substrate using

angle-resolved photoemission spectroscopy (ARPES). The interfacial interactions have been modified through the selective growth of structural phases ($1T$ and $1H$) of ML TaSe₂ using MBE. Strong interactions between ML $1H$ -TaSe₂ and BLG were evidenced by kinked band structures and significant charge transfer from BLG to TaSe₂, while weakly interacting ML $1T$ -TaSe₂ on BLG does not exhibit any charge transfer or band hybridization. The former deviates from the previous works that found the quasi-freestanding nature of MBE-grown ML TMDC on BLG [14–18]. Scanning tunneling microscopy (STM) measurements and first-principles calculations reveal differences in the atomic height and the modified work functions in the ML limit of two phases of TaSe₂, resulting in different electronic responses at the interface.

2 Results

Figure 1a presents the schematics for the controlled growth of ML TaSe₂ on a BLG substrate using MBE. It is well known that $1H$ - and $1T$ -TaSe₂ films can be selectively synthesized on BLG by controlling substrate temperature (T_{growth}) during the growth; low and high T_{growth} are suitable for the formation of $1H$ -TaSe₂ and $1T$ -TaSe₂, respectively [19]. Figure 1b and d show the ARPES spectra of MBE-grown ML TaSe₂ depending on T_{growth} . ARPES intensity maps demonstrate that the ML TaSe₂ film grown at high T_{growth} (= 750 °C) shows an insulating band structure (Fig. 1b) while the low T_{growth} (= 450 °C) shows metallic behavior (Fig. 1d). These results are consistent with the Mott insulating state by the Star-of-David (SoD) CDW transition in ML $1T$ -TaSe₂ and the metallic nature of ML $1H$ -TaSe₂, respectively [19, 22, 23]. On the other hand, the ML TaSe₂ film grown at intermediate T_{growth} (= 600 °C) exhibits mixed band structures of ML $1H$ - and $1T$ -TaSe₂ (Fig. 1c).

The selective fabrication of ML TaSe₂ films by controlling T_{growth} is also confirmed by core-level measurements since the change of crystal structures generates different crystal fields in TaSe₂ [23, 33, 34]. Figures 1e and f represent core-level spectra for Ta 4f and Se 3d, respectively. The peak shapes and positions of Ta 4f and Se 3d obtained from high T_{growth} = 750 °C (light blue) and low T_{growth} = 450 °C (dark blue) are in agreement with ones of $1T$ - and $1H$ -TaSe₂, respectively, as reported [35, 36]. On the other hand, for moderate T_{growth} = 600 °C, not only do multiple peaks appear in both Ta 4f and Se 3d, but they also have the same positions with the core peaks from $1T$ - and $1H$ -TaSe₂, indicating the coexistence of the $1H$ - and $1T$ -TaSe₂ islands. ARPES and core-level measurements demonstrate the importance of delicate control of T_{growth} to tune the structural phases of ML TaSe₂ on a BLG substrate [19, 23].

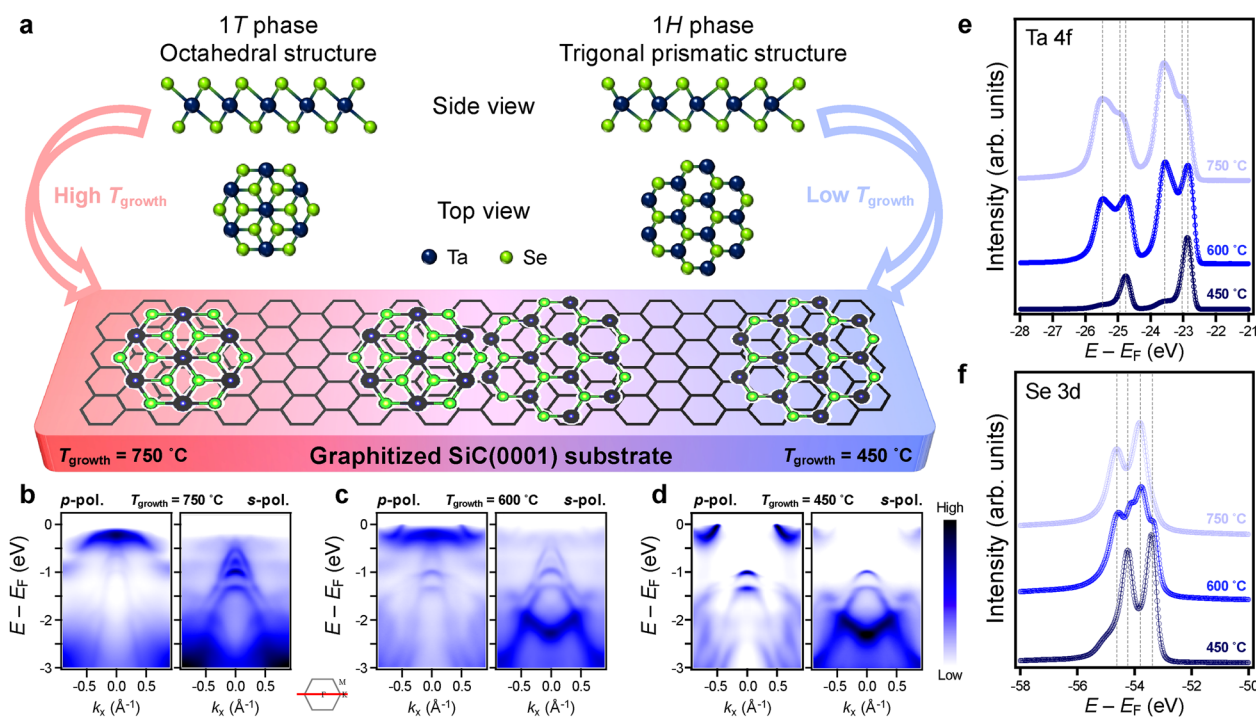


Fig. 1 Selective fabrications of 1T- and 1H-TaSe₂ on a BLG substrate. **a** Schematics of (top) Side- and top-view of atomic structures of TaSe₂ and (bottom) the T_{growth} dependent TaSe₂ film synthesis on a BLG substrate. **b-d** ARPES intensity maps of ML TaSe₂ films with three different T_{growth} . The formation of **b** ML 1T-TaSe₂ at $T_{\text{growth}} = 750$ °C, **c** mixed structures of ML TaSe₂ at $T_{\text{growth}} = 600$ °C, and **d** ML 1H-TaSe₂ at $T_{\text{growth}} = 450$ °C. The *p*- and *s*-polarized ARPES intensity maps were taken with 63 eV and 50 eV photons, respectively, at 10 K. **e-f** Core-level photoemission spectra from **e** Ta 4*f*- and **f** Se 3*d*-levels of ML TaSe₂ films. All the data were taken at 10 K

To investigate the effect of the BLG substrate on ML TaSe₂, the BLG π bands have been measured with and without overlaid TaSe₂ [37–40]. Figure 2a shows an ARPES intensity map of the BLG π bands without TaSe₂ taken at the K_G point perpendicular to the Γ_{G} –K_G direction of the Brillouin zone (BZ) of BLG. The obtained as-grown BLG π bands are intrinsically doped by electrons due to the presence of the SiC substrate [41]. The Dirac energy (E_{D}), defined here as the middle of the conduction band minimum and the valence band maximum, is located at ~ 0.3 eV below Fermi energy (E_{F}) extracted from the 2nd derivative ARPES spectrum (red lines) as shown in Fig. 2d. Figure 2b and e present the BLG π bands taken from fully covered ML 1T-TaSe₂ films. Compared to as-grown BLG on an SiC substrate (Fig. 2a), there are two non-dispersive states with weak spectral intensity located at 0.3 eV and 0.9 eV below E_{F} , which originate from ML 1T-TaSe₂ due to SoD CDW transition [42]. Although the additional bands are crossing the BLG π bands, the BLG π band dispersion is hardly changed. Moreover, we found a small amount of charge transfer from BLG to ML 1T-TaSe₂, i.e., a slight shift of E_{D} from 0.30 eV to 0.24 eV below E_{F} (Fig. 2e), indicating weak interactions between ML 1T-TaSe₂ and BLG.

On the other hand, remarkable changes are observed in BLG π bands when ML 1H-TaSe₂ is grown on a BLG substrate. As shown in Figs. 2c and 2f, ARPES intensity maps do not show the valence band maximum and E_{D} of BLG π bands. Extended straight lines over the upper π band give E_{D} at 0.135 eV above E_{F} . This result provides direct evidence of significant charge transfer from BLG to overlaid ML 1H-TaSe₂ [38, 39]. Moreover, BLG π bands show kinked structures at the crossing points with Ta 5*d* bands of 1H-TaSe₂ located at 0.1 eV and 0.38 eV below E_{F} [38] as denoted by orange and red dashed circles and arrows (Fig. 2f).

The charge transfer and the kinked structure are clearly resolved when the BLG π bands are taken along the K_G–M_G–K_G direction of the BZ of BLG. Figure 3a shows ARPES intensity maps of BLG π bands for 0.5 ML 1T-TaSe₂ on a BLG substrate, i.e., 50% of partial coverage of the substrate by 1T-TaSe₂. The coverage of ML TaSe₂ films was determined by comparing reflection high-energy electron diffraction (RHEED) intensity ratio between BLG and TaSe₂ peaks. As obtained in Fig. 2b and e, the BLG π bands do not show any kinked structure at the crossing points with ML 1T-TaSe₂ bands, and there are just two branches of BLG π bands due to the presence

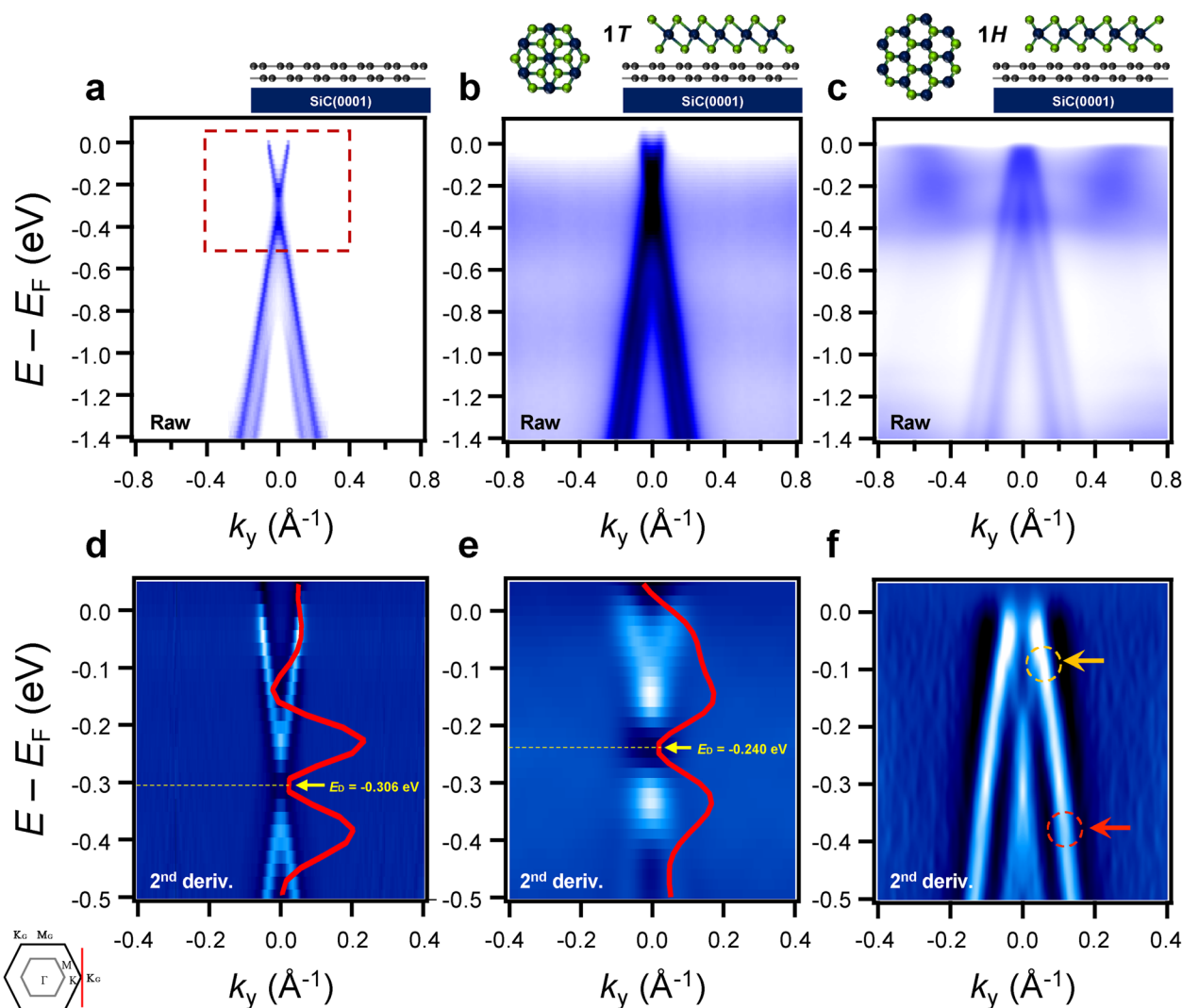


Fig. 2 ARPES spectra of BLG π bands with and without overlaid ML TaSe₂ films. **a–c** ARPES intensity maps of **a** as-grown BLG on SiC(0001), and BLG π bands covered with ML **b** 1T- and **c** 1H-TaSe₂ on a BLG substrate, respectively, taken at the K point of the BLG BZ (K_C) perpendicular to the Γ –K direction using p -polarized photons at 10 K. **d–f** Second derivative of the zoomed-in ARPES intensity maps (denoted by the red-dashed rectangle in panel **a**) for **d** as-grown BLG on SiC(0001), and BLG π bands covered with ML **e** 1T- and **f** 1H-TaSe₂ on a BLG substrate, respectively. Two non-dispersive bands with broad and weak spectral intensity at ~ 0.3 eV and ~ 0.9 eV below E_F in **b** originate from ML 1T-TaSe₂. The red curves in panels **d** and **e** are energy distribution curves of the second derivative maps taken at $k_y = 0.0 \text{ \AA}^{-1}$. The yellow dashed lines and arrows indicate E_D . The orange and red dashed circles and arrows in panel **f** represent kinked structures of BLG π bands. M_C (the M point of the BLG BZ) and K_C in the inset indicates the high symmetry points of BLG

of two layers of graphene [43]. We did not find any additional split of the BLG π band (Fig. 3a and d), indicating negligible interactions. On the other hand, the 0.5 ML 1H-TaSe₂ sample exhibits three branches of BLG π bands as denoted by yellow arrows in Fig. 3b and e. These multiple branches stem from the partial coverage (0.5 ML) of 1H-TaSe₂ films on BLG substrate and ARPES measurements simultaneously catch BLG π bands from both as-grown BLG/SiC(0001) and 1H-TaSe₂ on BLG/SiC(0001) due to finite spot size of the photon beam [18, 23, 33].

Indeed, for the nearly full coverage of 1H-TaSe₂ on a BLG substrate (Fig. 3c and f), the BLG π bands are reduced to two branches, which are shifted toward E_F because of charge transfer from BLG to ML 1H-TaSe₂. Concomitantly, there is a discontinuity in the upper π band of BLG at 1.5 eV below E_F , as denoted by black-dashed circles in Fig. 3b, c and e–f. Such changes, e.g., charge transfer and kinked structures, indicate that there exist strong interactions between ML 1H-TaSe₂ and a BLG substrate [37–41].

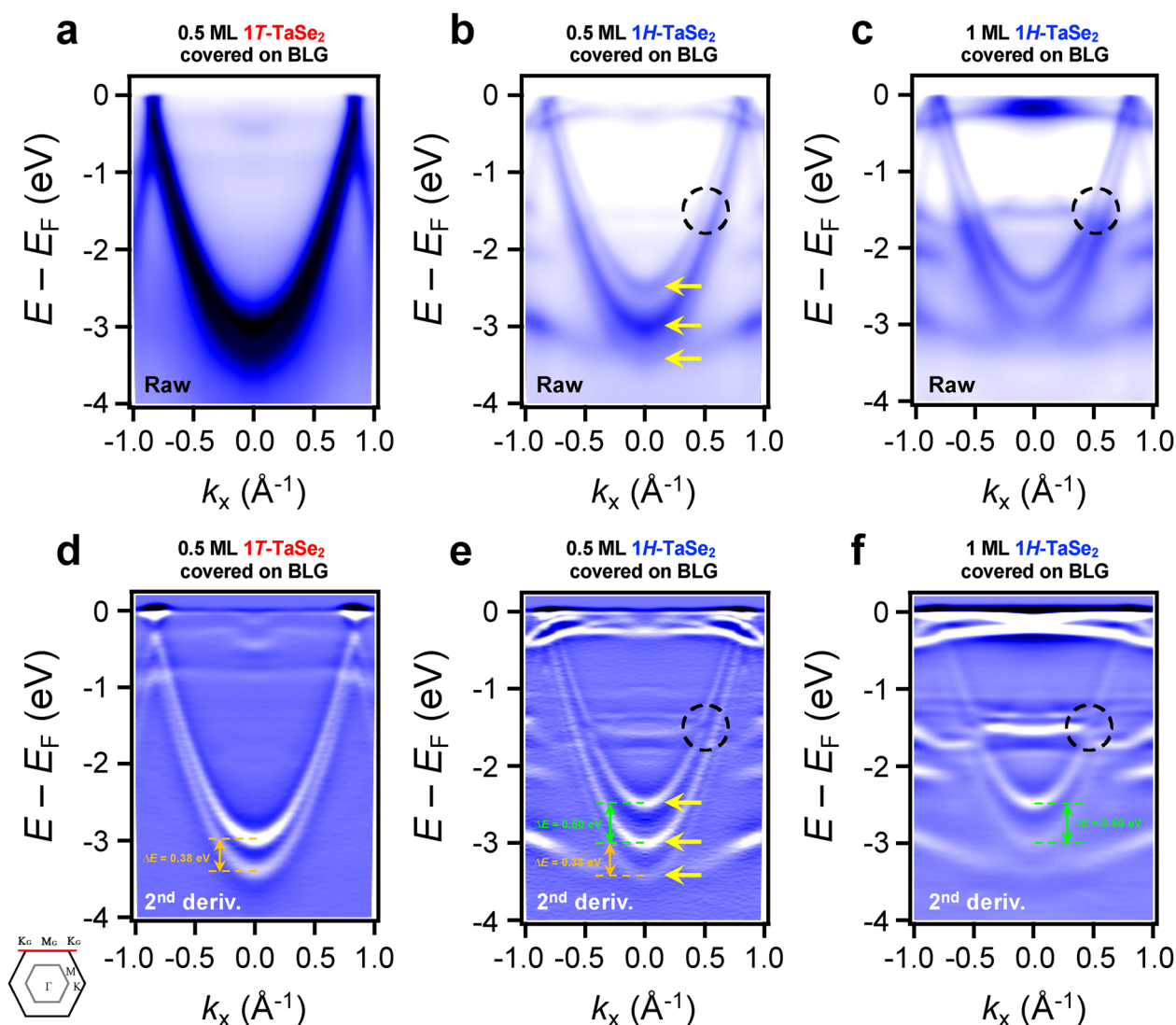


Fig. 3 Comparison of the effect of the crystal structure of ML TaSe₂ films on the BLG substrate. **a–c** ARPES data of BLG π bands taken along the K_{Γ} – M_{Γ} – K_{Γ} direction of the BZ of BLG. **d–f** The second derivatives of ARPES data in panels **a–c**. All ARPES data were taken using p -polarized photons at 10 K to better visualize the BLG π bands. The black dashed circles denote the kinked structures of BLG π bands. Yellow arrows represent the split of BLG π bands at the M_{Γ} point. Green and orange arrows, and dashed lines indicate the splitting size of the BLG π bands (ΔE)

BLG π bands at the M_{Γ} point reveal another intriguing evidence of the charge transfer between ML $1H$ -TaSe₂ and a BLG substrate. We found that the split of upper and lower BLG π bands shows different split energy values (ΔE) depending on the overlaid ML TaSe₂ crystal structures. The split of the lower two branches in Fig. 3e has $\Delta E = 0.38$ eV, which is comparable to one of the as-grown BLG π bands on a SiC substrate [43] and of ML $1T$ -TaSe₂ on BLG (Fig. 3d). On the other hand, the upper two branches of BLG π bands in Fig. 3e has $\Delta E = 0.50$ eV, which corresponds to the hole-doped ML $1H$ -TaSe₂ on BLG (Fig. 3f). The enhanced ΔE may originate from the inequivalent

charge distribution in the upper and lower BLG layers [43, 44]. While the lower graphene layer takes the electrons from the SiC substrate, the upper layer transfers the electrons to ML $1H$ -TaSe₂ [44], as evidenced in ARPES results (Figs. 2 and 3). The sufficient asymmetry of the charge density between the BLG layers induces the field at the respective interfaces, resulting in the enhancement of ΔE [44].

3 Discussion

The selective interactions in ML TaSe₂ films on BLG are non-trivial, because it is reasonable to expect similar amount of charge transfer in both structural phases of

TaSe₂, considering the work function difference between BLG (4.3 eV) and bulk TaSe₂ (5.1 eV for 1*T* and 5.5 eV for 2*H*) [45–47]. However, the work function can be modified when TaSe₂ is thinned down to ML [46–50]. The calculated work functions for 1*H*-TaSe₂ are hardly changed from bulk (5.5 eV) to ML (5.45 eV), whereas the work function of 1*T*-TaSe₂ are significantly reduced from bulk (5.10 eV) to ML (4.66 eV) (Fig. 4a). The difference in the charge transfer between TaSe₂ and BLG is due to the distinct behavior of the work function in the 2D limit of 1*T* and 1*H* phases of TaSe₂.

In addition, an interlayer distance between TaSe₂ and BLG can also play a crucial role in the electronic properties at the interface, since the Schottky barrier is modified as a function of the distance of vdW layers [51–55]. Our STM measurements reveal that MBE-grown ML 1*T*- and 1*H*-TaSe₂ on a BLG substrate show a different height of 1.02 nm and 0.85 nm, respectively (Fig. 4b, c). In general, height estimated from STM topography reflects atomic positions in real space as well as contributions from electronic structures. A height difference of 1.7 Å in STM data thus implies either that the vdW gap between ML 1*T*-TaSe₂ and BLG is wider by ~ 1.7 Å or that 1*H*-TaSe₂ has much lower density of states (DOS) so that the tip must move towards the 1*H*-TaSe₂ film (compared to 1*T*-TaSe₂) to maintain the same tunneling condition at certain sample bias voltage (V_b) [56]. Since the DOS taken at $V_b = -1$ V is larger in ML 1*H*-TaSe₂ than ML 1*T*-TaSe₂ [25, 57, 58], however, the obtained STM heights provide evidence of the shorter vdW gap between ML 1*H*-TaSe₂ and BLG, compared to that of ML 1*T*-TaSe₂. Hence, our findings suggest that the strong (weak) interactions between ML 1*H* (1*T*)-TaSe₂ and a BLG substrate originate from the dual effects of the significant (small)

work function difference and the relatively shorter (larger) interlayer distances.

4 Conclusions

In summary, we have investigated the electronic structure of the ML TaSe₂ on BLG when the structural phase of TaSe₂ is selectively grown in a controlled way. The presence of ML 1*H*-TaSe₂ on BLG results in strong interactions evidenced by the energy shift due to hole doping in the BLG band structure and the kinked structure at the band crossing points between ML 1*H*-TaSe₂ and BLG. On the other hand, the presence of ML 1*T*-TaSe₂ on BLG shows nearly negligible effects on the BLG band structure, indicating weak interactions. The distinct response from ML 1*H*- and 1*T*- TaSe₂ on BLG originate from reduced interfacial distance and strongly reduced work function of 1*H*-TaSe₂ in the ML limit. Our findings provide an exceptional example of strong interactions between the BLG substrate and an epitaxially-grown TMDC material, which paves the way for discovering and manipulating novel electronic phases in 2D vdW materials and their heterostructures.

5 Methods

5.1 Thin film growth and in-situ ARPES measurement

The BLG substrate was prepared by flashing annealing of the 6H-SiC(0001) at 1300 °C for 60 cycles. The ML 1*H*- and 1*T*-TaSe₂ films were grown by molecular beam epitaxy (MBE) on epitaxial bilayer graphene on 6H-SiC(0001). The base pressure of the MBE chamber was 3×10^{-10} Torr. High-purity Ta (99.99%) and Se (99.999%) were evaporated from an e-beam evaporator and a standard Knudsen effusion cell, respectively. The flux ratio was fixed as Ta:Se = 1:10, and the BLG substrate

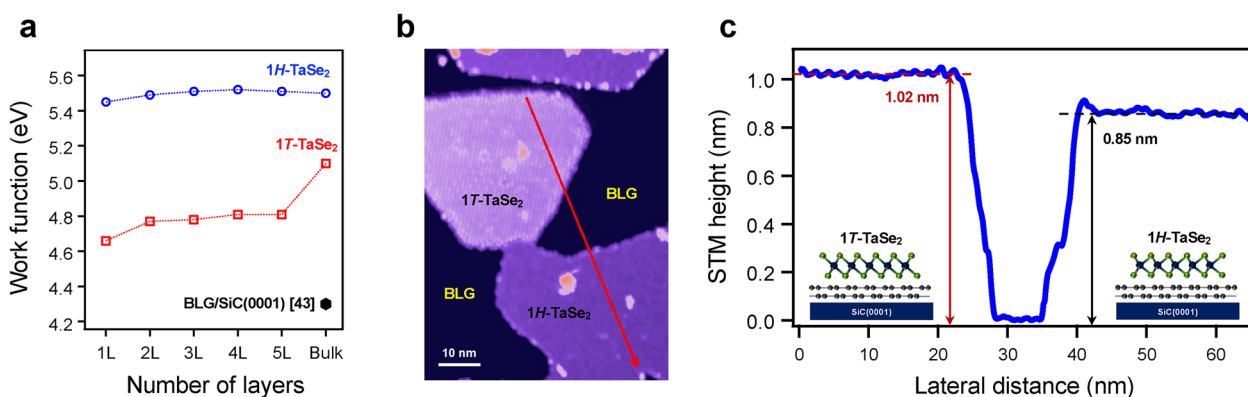


Fig. 4 Thickness-dependent work function and STM step height of ML TaSe₂ films on BLG. **a** The calculated work function of few-layer 1*T*-TaSe₂ (red) and 1*H*-TaSe₂ (blue). **b** STM topographic image with islands of both ML 1*T*-TaSe₂ (light purple) and 1*H*-TaSe₂ (deep purple) on a BLG/SiC(0001) substrate (scanned at sample bias $V_b = -1$ V and tunnelling current $I_t = 5$ pA at 5 K). **c** An STM height profile taken along a red arrow shown in panel **b**

temperatures were ranged from 450 °C (1H-TaSe₂) to 750 °C (1T-TaSe₂). This yields a growth rate of 40 mins per ML monitored by *in situ* Reflection high-energy electron diffraction (RHEED).

The MBE-grown ML TaSe₂ films were transferred directly into the ARPES analysis chamber for the measurement at the HERS endstation of Beamline 10.0.1, Advanced Light Source, Lawrence Berkeley National Laboratory. ARPES data were taken using a Scienta R4000 analyzer at base pressure 3×10^{-11} Torr. The photon energies were set at 50 eV for *s*-polarizations and 63 eV for *p*-polarizations with energy and angular resolution of 10–20 meV and 0.1°, respectively. The spot size of the photon beam on the sample was $\sim 100 \mu\text{m} \times 100 \mu\text{m}$. Se capping layers of ~ 100 nm were deposited onto ML TaSe₂ films at room temperature to prevent contamination during transport through air to the ultrahigh vacuum (UHV) scanning tunneling microscopy (STM) chamber. Se capping layers were removed by annealing the sample to 200 °C overnight in the UHV before the STM measurements.

5.2 STM measurement

STM measurements are performed using a commercial Omicron LT-STM/AFM under UHV conditions at $T = 5$ K with tungsten tips. STM topography was obtained in constant-current mode. STM tips were calibrated on an Au(111) surface by measuring the Au(111) Shockley surface state before all STS measurements. STS was performed under open feedback conditions by lock-in-detection of an alternating-current tunnel current with a small bias modulation at 401 Hz added to the tunneling bias. WSxM software was used to process the STM images.

5.3 Density functional theory calculation

Work function calculations were conducted using the density functional theory method with the Quantum ESPRESSO package [59]. We employed the generalized gradient approximation (GGA) of Perdew, Burke, and Ernzerhof (PBE) functionals [60]. A plane wave kinetic energy cutoff of 100 Ry (1360 eV) and $12 \times 12 \times 1$ Monkhorst–Pack mesh were employed [61]. A vacuum gap thickness of 20 Å was introduced at the side of the slab for all systems to calculate the work function ($\phi = V_{vac} - E_F$). All work function values were extracted from the plane-averaged electrostatic potential.

Abbreviations

2D	Two-dimension
MBE	Molecular beam epitaxy
TMDC	Transition metal dichalcogenides
BLG	Bilayer graphene
vdW	Van der Waals
ML	Monolayer
CDW	Charge density wave

ARPES	Angle-resolved photoemission spectroscopy
STM	Scanning tunneling microscopy
T_{growth}	Substrate temperature during the growth
SoD	Star-of-David
BZ	Brillouin zone
E_D	Dirac energy
E_F	Fermi energy
ΔE	Split energy values
V_b	Bias voltage

Acknowledgements

The work at ALS (ARPES) is supported by the US DoE Office of Basic Energy Science under contract No. DE-AC02-05CH11231. The work at UC Berkeley (STM) is supported by the US National Science Foundation grant No. DMR-2221750. The work at KNU is supported by the National Research Foundation of Korea (NRF) grant funded by the Korean government (MSIT) (RS-2023-00280346), the GRDC (Global Research Development Center) Cooperative Hub Program through the NRF funded by the Ministry of Science and ICT (MIST) (RS-2023-00258359), and Semiconductor R&D Support Project through the Gangwon Technopark (GWTP) funded by Gangwon Province (No. GWTP 2023-027). The work at PNU is supported by the NRF of Korea (No. 2021R1A2C1004266 and No. RS-2023-00221154) and the National Research Facilities and Equipment Center (NFEC) grant funded by the Ministry of Education (No. 2021R1A6C101A429). Max Planck POSTECH/Korea Research Initiative is supported by the NRF of Korea (2022M3H4A1A04074153). J.-E.L. is partially supported by the ALS collaborative Postdoctoral Fellowship. Y.C. acknowledges support from the National Natural Science Foundation of China (Grant No. 12250001 and 92365114). W.R. acknowledges financial support from the National Science Foundation of China (Grant No. 12274087) and Shanghai Science and Technology Development Funds (Grant No. 22QA1400600). B.K.C. acknowledges supports from NRF (2021R1A6A3A14040322). The authors acknowledge the Urban Big data and AI Institute of the University of Seoul supercomputing resources. H.R. acknowledges support from KIST Institutional Program (2E32951) and NRF grant funded by the Korea government (MSIT) (No. 2021R1A2C2014179 and 2020R1A5A1016518).

Author contributions

JH, CH, SKM proposed and designed the research. JW performed film growth with assistance from HL, HI, KP, and L-EL. JW, HL, HI, YZ, and HR carried out the ARPES measurements and analyzed the ARPES data with assistance from CH, ZXS, and SKM. YC and WR carried out the STM measurements with assistance from MFC. BKC performed the DFT calculations. HL, HI, and JH wrote the manuscript and revised it with assistance from CH and SKM. All authors contributed to the scientific planning and discussions.

Data availability

The data that support the plots within this paper and other findings of this study are available from the corresponding authors upon reasonable request.

Declarations

Competing interests

The authors declare no competing interests.

Received: 12 February 2024 Accepted: 1 April 2024

Published online: 15 April 2024

References

1. K.S. Novoselov, A. Mishchenko, A. Carvalho, A.H. Castro Neto, *Science* **353**, 6298 (2016)
2. S.-K. Mo, *Nano Converg.* **4**, 6 (2017)
3. J.A. Sobota, Y. He, Z.-X. Shen, *Rev. Mod. Phys.* **93**, 025006 (2021)
4. J.-E. Lee, Kyoo Kim, V. Q. Nguyen, J. Hwang, J. D. Denlinger, B. I. Min, S. Cho, H. Ryu, C. Hwang, S.-K. Mo, *Nano Converg.* **10**, 32 (2023)
5. H. Lu, W. Liu, H. Wang, X. Liu, Y. Zhang, D. Yang, X. Pi, *Nanotechnology* **34**, 132001 (2023)

6. L.A. Walsh, C.L. Hinkle, *Appl. Mater. Today* **9**, 504–515 (2017)
7. J. Wang, T. Li, Q. Wang, R. Shi, N. Wang, A. Amini, C. Cheng, *Mater. Today Adv.* **8**, 100098 (2020)
8. H. J. Kim, M. Chong, T. G. Rhee, Y. G. Khim, M.-H. Jung, Y.-M. Kim, H. Y. Jeong, B. K. Choi, Y. J. Chang, *Nano Converg.* **10**, 10 (2023)
9. A. Wang, Z. Liu, J. Pan, Q. Li, G. Li, Q. Huan, S. Du, H.-J. Gao, *Chin. Phys. B* **29**, 078102 (2020)
10. M.-K. Lin, J.A. Hlevyack, P. Chen, R.-Y. Liu, S.-K. Mo, T.-C. Chiang, *Phys. Rev. Lett.* **125**, 176405 (2020)
11. P. Dreher, W. Wan, A. Chikina, M. Bianchi, H. Guo, R. Harsh, S. Manas-Valero, E. Coronado, A.J. Martínez-Galera, P. Hofmann, J.A. Miwa, M.M. Ugeda, *ACS Nano* **15**, 19430–19438 (2021)
12. T. Jia, S.N. Rebec, S. Tang, K. Xu, H.M. Sohail, M. Hashimoto, D. Lu, R.G. Moore, Z.-X. Shen, *2D Mater.* **6**, 011008 (2019)
13. W. Chen, M. Hu, J. Zong, X. Xie, Q. Meng, F. Yu, L. Wang, W. Ren, A. Chen, G. Liu, X. Xi, F.-S. Li, J. Sun, J. Liu, Y. Zhang, *Adv. Mater.* **33**, 2004930 (2021)
14. Y. Zhang, T.-R. Chang, B. Zhou, Y.-T. Cui, H. Yan, Z. Liu, F. Schmitt, J. Lee, R. Moore, Y. Chen, H. Lin, H.-T. Jeng, S.-K. Mo, Z. Hussain, A. Bansil, Z.-X. Shen, *Nat. Nanotechnol.* **9**, 111–115 (2014)
15. Y. Song, C. Jia, H. Xiong, B. Wang, Z. Jiang, K. Huang, J. Hwang, Z. Li, C. Hwang, Z. Liu, D. Shen, J.A. Sobota, P. Kirchmann, J. Xue, T.P. Devereaux, S.-K. Mo, Z.-X. Shen, S. Tang, *Nat. Commun.* **14**, 11116 (2023)
16. S. Tang, C. Zhang, D. Wong, Z. Pedramrazi, H.-Z. Tsai, C. Jia, B. Moritz, M. Claassen, H. Ryu, S. Kahn, J. Jiang, H. Yan, M. Hashimoto, D. Lu, R.G. Moore, C.-C. Hwang, C. Hwang, Z. Hussain, Y. Chen, M.M. Ugeda, Z. Liu, X. Xie, T.P. Devereaux, M.F. Crommie, S.-K. Mo, Z.-X. Shen, *Nat. Phys.* **13**, 683–687 (2017)
17. J. Hwang, K. Kim, C. Zhang, T. Zhu, C. Herbig, S. Kim, B. Kim, Y. Zhong, M. Salah, M.M. El-Desoky, C. Hwang, Z.-X. Shen, M.F. Crommie, S.-K. Mo, *Nat. Commun.* **13**, 906 (2022)
18. J. Hwang, Y. Jin, C. Zhang, T. Zhu, K. Kim, Y. Zhong, J.-E. Lee, Z. Shen, Y. Chen, W. Ruan, H. Ryu, C. Hwang, J. Lee, M.F. Crommie, S.-K. Mo, Z.-X. Shen, *Adv. Mater.* **34**, 2204579 (2022)
19. Y. Nakata, T. Yoshizawa, K. Sugawara, Y. Uemoto, T. Takahashi, T. Sato, *A.C.S. Appl. Nano Mater.* **1**, 1456–1460 (2018)
20. S.C. de la Barrera, M.R. Sinko, D.P. Gopalan, N. Sivasdas, K.L. Seyler, K. Watanabe, T. Taniguchi, A.W. Tsien, X. Xu, D. Xiao, B.M. Hunt, *Nat. Commun.* **9**, 1427 (2018)
21. M.M. Ugeda, A.J. Bradley, Y. Zhang, S. Onishi, Y. Chen, W. Ruan, C. Ojeda-Aristizabal, H. Ryu, M.T. Edmonds, H.-Z. Tsai, A. Riss, S.-K. Mo, D. Lee, A. Zettl, Z. Hussain, Z.-X. Shen, M.F. Crommie, *Nat. Phys.* **12**, 92–97 (2016)
22. H. Ryu, Y. Chen, H. Kim, H.-Z. Tsai, S. Tang, J. Jiang, F. Liou, S. Kahn, C. Jia, A.A. Omrani, J.H. Shim, Z. Hussain, Z.-X. Shen, K. Kim, B.I. Min, C. Hwang, M.F. Crommie, S.-K. Mo, *Nano Lett.* **18**, 689–694 (2018)
23. Y. Chen, W. Ruan, M. Wu, S. Tang, H. Ryu, H.-Z. Tsai, R.L. Lee, S. Kahn, F. Liou, C. Jia, O.R. Albertini, H. Xiong, T. Jia, Z. Liu, J.A. Sobota, A.Y. Liu, J.E. Moore, Z.-X. Shen, S.G. Louie, S.-K. Mo, M.F. Crommie, *Nat. Phys.* **16**, 218–224 (2020)
24. Y. Chen, W.-Y. He, W. Ruan, J. Hwang, S. Tang, R.L. Lee, M. Wu, T. Zhu, C. Zhang, H. Ryu, F. Wang, S.G. Louie, Z.-X. Shen, S.-K. Mo, P.A. Lee, M.F. Crommie, *Nat. Phys.* **18**, 1335–1340 (2022)
25. W. Ruan, Y. Chen, S. Tang, J. Hwang, H.-Z. Tsai, R.L. Lee, M. Wu, H. Ryu, S. Kahn, F. Liou, C. Jia, A. Aikawa, C. Hwang, F. Wang, Y. Choi, S.G. Louie, P.A. Lee, Z.-X. Shen, S.-K. Mo, M.F. Crommie, *Nat. Phys.* **17**, 1154–1161 (2021)
26. M. Liu, J. Leveillee, S. Lu, J. Yu, H. Kim, C. Tian, Y. Shi, K. Lai, C. Zhang, F. Giustino, C.-K. Shih, *Sci. Adv.* **7**, eabi6339 (2021)
27. V. Vano, M. Amini, S.C. Ganguli, G. Chen, J.L. Lado, S. Kezilebieke, P. Liljeroth, *Nature* **599**, 582–586 (2021)
28. W. Wan, R. Harsh, A. Meninno, P. Dreher, S. Sajan, H. Guo, I. Errea, F. de Juan, M.M. Ugeda, *Nat. Commun.* **14**, 7005 (2023)
29. J. W. Park, H. W. Yeom, *arXiv preprint arXiv:2008.05702* (2020)
30. J.W. Park, H.W. Yeom, *ACS Nano* **17**, 17041–17047 (2023)
31. C.-E. Ahn, K.-H. Jin, J. W. Park, H. W. Yeom, A. Go, Y. B. Kim, G. Y. Cho, *arXiv preprint arXiv:2309.15916* (2023)
32. S.-Z. Wang, Y.-M. Zhang, J.-Q. Fan, M.-Q. Ren, C.-L. Song, X.-C. Ma, Q.K. Xue, *Phys. Rev. B* **102**, 241408(R) (2020)
33. M.M. Ugeda, A. Pulkin, S. Tang, H. Ryu, Q. Wu, Y. Zhang, D. Wong, Z. Pedramrazi, A. Martín-Recio, Y. Chen, F. Wang, Z.-X. Shen, S.-K. Mo, O.V. Yazyev, M.F. Crommie, *Nat. Commun.* **9**, 3401 (2018)
34. S. Cho, S. Kim, J.H. Kim, J. Zhao, J. Seok, D.H. Keum, J. Baik, D.-H. Choe, K.J. Chang, K. Suenaga, S.W. Kim, Y.H. Lee, H. Yang, *Science* **349**, 625–628 (2015)
35. Y. Nakata, K. Sugawara, A. Chainani, H. Oka, C. Bao, S. Zhou, P.-Y. Chuang, C.-M. Cheng, T. Kawakami, Y. Saruta, T. Fukumura, S. Zhou, T. Takahashi, T. Sato, *Nat. Commun.* **12**, 5873 (2021)
36. H.E. Brauer, H.I. Starnberg, L.J. Holleboom, H.P. Hughes, V.N. Strocov, J. Phys. Condens. Matter **13**, 9879–9895 (2001)
37. J. Hwang, N.-K. Chung, A.D. N'Diaye, J. Denlinger, A.K. Schmid, C. Hwang, J. Kor. Phys. Soc. **69**, 573–577 (2016)
38. J. Hwang, H. Hwang, M.-J. Kim, H. Ryu, J.-E. Lee, Q. Zhou, S.-K. Mo, J. Lee, A. Lanzara, C. Hwang, *Nanoscale* **9**, 11498 (2017)
39. J. Hwang, S. Lee, J.-E. Lee, M. Kang, H. Ryu, H. Joo, J. Denlinger, J.-H. Park, C. Hwang, *Nano Lett.* **20**, 7973–7979 (2020)
40. A. Varykhalov, J. Sánchez-Barriga, D. Marchenko, P. Hlawenka, P.S. Mandal, O. Rader, *Nat. Commun.* **6**, 7610 (2015)
41. J. Hwang, C. Hwang, *New J. Phys.* **18**, 043005 (2016)
42. K. Rossnagel, *J. Phys. Condens. Matter* **23**, 213001 (2011)
43. T. Ohta, A. Bostwick, T. Seyller, K. Horn, E. Rotenberg, *Science* **313**, 951–954 (2006)
44. A. Bostwick, J. McChesney, T. Ohta, E. Rotenberg, T. Seyller, K. Horn, *Progress Surf. Sci.* **84**, 380–413 (2009)
45. S. Mammadov, J. Ristein, J. Krone, C. Raidel, M. Wanke, V. Wiesmann, F. Speck, T. Seyller, *2D Mater.* **4**, 015043 (2017)
46. H.-S. Tsai, F.-W. Liu, J.-W. Liou, C.-C. Chi, S.-Y. Tang, C. Wang, H. Ouyang, Y.-L. Chueh, C. Liu, S. Zhou, W.-Y. Woon, *ACS Omega* **4**, 17536–17541 (2019)
47. C. Pettenkofer, W. Jaegermann, A. Schellenberger, E. Holub-Krappe, *Solid State Commun.* **84**, 921–926 (1992)
48. C. Zhang, C. Gong, Y. Nie, K.-A. Min, C. Liang, Y.J. Oh, H. Zhang, W. Wang, S. Hong, L. Colombo, R.M. Wallace, K. Cho, *2D Mater.* **4**, 015026 (2017)
49. H.-G. Kim, H.J. Choi, *Phys. Rev. B* **103**, 085404 (2021)
50. Y. Cai, G. Zhang, Y.-W. Zhang, *Sci. Rep.* **4**, 6677 (2014)
51. Y. Jiao, A. Hellman, Y. Fang, S. Gao, M. Käll, *Sci. Rep.* **5**, 11374 (2015)
52. X. Zhu, H. Jiang, Y. Zhang, D. Wang, L. Fan, Y. Chen, X. Qu, L. Yang, Y. Liu, *Molecules* **28**, 5607 (2023)
53. D.J. Rizzo, S. Shabani, B.S. Jessen, J. Zhang, A.S. McLeod, C. Rubio-Verdú, F.L. Ruta, M. Cothrine, J. Yan, D.G. Mandrus, S.E. Nagler, A. Rubio, J.C. Hone, C.R. Dean, A.N. Pasupathy, D.N. Basov, *Nano Lett.* **22**, 1946–1953 (2022)
54. Y. Li, J. Wang, B. Zhou, F. Wang, Y. Miao, J. Wei, B. Zhang, K. Zhang, *Phys. Chem. Chem. Phys.* **20**, 24109–24116 (2018)
55. R. Zhang, G. Hao, X. Ye, S. Gao, H. Li, *Phys. Chem. Chem. Phys.* **22**, 23699–23706 (2020)
56. C.J. Chen, *Introduction to scanning tunneling microscopy*, vol. 69, 3rd edn. (Oxford University Press, Oxford, 2021)
57. J.-A. Yan, M.A. Dela Cruz, B. Cook, K. Varga, *Sci. Rep.* **5**, 16646 (2015)
58. D.C. Miller, S.D. Mahanti, P.M. Duxbury, *Phys. Rev. B* **97**, 045133 (2018)
59. P. Giannozzi, S. Baroni, N. Bonini, M. Calandra, R. Car, C. Cavazzoni, D. Ceresoli, G.L. Chiarotti, M. Cococcioni, I. Dabo, A.D. Corso, S. de Gironcoli, S. Fabris, G. Fratesi, R. Gebauer, U. Gerstmann, C. Gougousis, A. Kokalj, M. Lazzeri, L. Martin-Samos, N. Marzari, F. Mauri, R. Mazzarello, S. Paolini, A. Pasquarello, L. Paulatto, C. Sbraccia, S. Scandolo, G. Sclauzero, A.P. Seitsonen, A. Smogunov, P. Umari, R.M. Wentzcovitch, *J. Phys. Condens. Matter* **21**, 395502 (2009)
60. J.P. Perdew, K. Bruke, M. Ernzerhof, *Phys. Rev. Lett.* **77**, 3865 (1996)
61. H.J. Monkhorst, J.D. Pack, *Phys. Rev. B* **13**, 5188 (1976)

Publisher's Note

Springer Nature remains neutral with regard to jurisdictional claims in published maps and institutional affiliations.